A Theory for Self-Sustained Multicentennial Oscillation of the Atlantic Meridional Overturning Circulation

YANG LI[a] AND HAIJUN YANG[b,c]

[a] Department of Atmospheric and Oceanic Sciences, School of Physics, Peking University, Beijing, China
[b] Department of Atmospheric and Oceanic Sciences and Institute of Atmospheric Science and CMA-FDU Joint Laboratory of Marine Meteorology, Fudan University, Shanghai, China
[c] Shanghai Scientific Frontier Base for Ocean–Atmosphere Interaction Studies, Fudan University, Shanghai, China

(Manuscript received 1 September 2021, in final form 4 May 2022)

ABSTRACT: In this work, a single-hemisphere 4-box model is used to study the low-frequency variability of the Atlantic meridional overturning circulation (AMOC). We introduce an enhanced mixing mechanism in the subpolar ocean to balance the positive salinity advection feedback, so that the AMOC in the 4-box model exhibits a self-sustained multicentennial oscillation. The enhanced mixing mechanism is proposed based on results from a coupled climate model, which show that the eddy-induced mixing or diffusion in the subpolar ocean is always enhanced when the AMOC anomaly is large; namely, the enhancement is due to weak stratification when the AMOC is strong, and is due to mesoscale and submesoscale eddies when the AMOC is weak. Without the enhanced mixing, the 4-box model system can be either stable or unstable, but cannot realize a self-sustained stable oscillation. With the enhanced mixing, the 4-box model can be interpreted approximately as a reduced 3-box model, so that the theoretical solution to the multicentennial oscillation can be obtained. The oscillation period is determined by the eigenvalue of the system, which is fundamentally controlled by the turnover time of the upper ocean. We also illustrate that the multicentennial oscillation can be excited by stochastic freshwater forcing. This study suggests that the Atlantic Ocean has an intrinsic multicentennial mode, which may help us understand this class of variability identified in paleoclimatic proxy data.

KEYWORDS: Convection; Ocean dynamics; Thermocline circulation; Oscillations; Meridional overturning circulation

1. Introduction

Earth's climate system has multicentennial time-scale variability, evidenced by paleoclimatic reconstruction data from tree rings, ice core, and sediments in lakes and oceans as well as by historical documents from Europe, Asia, and America (e.g., Sirén 1961; Soutar and Isaacs 1969; Johnsen et al. 1970; LaMarche 1974; Fisher 1982; Gajewski 1988; Stuiver and Braziunas 1989; Stocker and Mysak 1992; Chapman and Shackleton 2000; Risebrobakken et al. 2003; Zheng et al. 2010). Multicentennial variability has been observed in land precipitation, ocean temperature, salinity, and currents. Particularly, many proxies obtained in the North Atlantic region are thought to be associated with historical events such as the Medieval Climatic Anomaly (MCA) and the Little Ice Age (LIA) (e.g., Cronin et al. 2010; Sicre et al. 2011; Miettinen et al. 2015; Moffa-Sánchez et al. 2015), which, in turn, suggest multicentennial variability of the Atlantic meridional overturning circulation (AMOC). In this paper, multicentennial time scale refers to the time scale of about 500 ± 300 years. Centennial variability (about 100 years) and millennial variability are not our foci.

The origin and mechanism of multicentennial variability have been challenging topics for scientists, due to the lack of observational data and complexities of internal processes, external forcing, and their interactions. For example, although many coupled model simulations showed that solar irradiance dominates internal variabilities at multidecadal and longer time scales and at large spatial scales (Cubasch et al. 1997; Drijfhout et al. 1999; Rind et al. 1999), studies also suggested that at the multicentennial time scale the internal feedback processes, especially the delayed advection–salinity feedback, seem to play an important role, and the solar irradiance acts more as an initial stimulation (Weber et al. 2004). More specifically, many studies supported the idea that the LIA was triggered by external forcing, such as solar irradiance variation and volcanic clusters (Berner et al. 2011; Miller et al. 2012). However, results from coupled model sensitivity experiments suggested that volcanic forcing is not a prerequisite (Moreno-Chamarro et al. 2017). Modeling studies suggested that the forced signal only accounts for 10%–35% of the total variance of the signals longer than 10 years in the past two millennia (Moffa-Sánchez et al. 2019).

Assessing the relative roles of external forcing and internal processes in multicentennial variability is critical to unravel the mystery of historical events such as the MCA and LIA. Above all, an in-depth investigation of multicentennial internal variability is needed first. This also helps climate prediction, as the magnitude of global warming over the last 6–7 decades may have been damped by internal variability from the Atlantic Ocean (Bonnet et al. 2021). The ocean is believed to govern the multicentennial variability, due to the integration of short-term atmosphere fluctuations and its internal dynamics related to the thermohaline circulation (THC) or the

Denotes content that is immediately available upon publication as open access.

Corresponding author: Haijun Yang, yanghj@fudan.edu.cn

DOI: 10.1175/JCLI-D-21-0685.1

AMOC (Mikolajewicz and Maier-Reimer 1990; Msadek and Frankignoul 2008). Besides, a better understanding and representation of the multicentennial AMOC variability may help improve the decadal predictability of Earth's climate (Collins and Sinha 2003).

There have been many studies on the multicentennial mode of the climate system, using a hierarchy of models of different complexities, ranging from simple energy balance models to coupled general circulation models (GCMs) (e.g., Welander 1982; Mikolajewicz and Maier-Reimer 1990; Mysak et al. 1993; Sévellec et al. 2006; Sévellec and Fedorov 2014; Jiang et al. 2021). In an earlier study using an ocean GCM (OGCM), Mikolajewicz and Maier-Reimer (1990) identified a 320-yr mode, which stands out most clearly in the strength of the Antarctic circumpolar current, and its period agrees well with the overall flushing time of the Atlantic Ocean. This mode is attributed to salinity anomaly advection by the AMOC, driven by the deep-water formation in the Weddell Sea. Mysak et al. (1993) found a similar mode under random freshwater flux in a two-dimensional ocean model representing the Atlantic Ocean; they also emphasized the importance of the transport of salinity anomalies. In this paper, we are mainly interested in the multicentennial mode of the AMOC in simple box models, because we aim for fundamental understanding via theoretical study.

In modeling studies using simple models, low-frequency oscillations can emerge from either external forcing or internal processes. The former can be classified as the forced oscillatory, in which the low-frequency variability is attributed to the response of the AMOC to stochastic atmosphere forcing (Griffies and Tziperman 1995; Roebber 1995). Both the spatial pattern and spectrum of atmospheric forcing can influence the period of AMOC oscillation (Tziperman and Ioannou 2002). The latter is classified as the self-sustained oscillation, in which the ocean itself can generate self-sustained oscillation (e.g., Rivin and Tziperman 1997, hereafter RT97). In fact, in the earlier study of Welander (1982), a self-sustained oscillation was realized by introducing a "flip-flop" local convection mechanism, which was then applied to describe millennial thermohaline oscillation (e.g., Zhang et al. 2002; Colin de Verdière et al. 2006). While these studies concentrated on multiple equilibrium states, they reminded us that the local vertical density profile may influence the large-scale overturning circulation. Salinity advection feedback can also be an energy source; for example, a strong AMOC will make the subpolar ocean more saline and thus denser, which in turn leads to a stronger AMOC. In RT97, a self-sustained oscillation was identified after introducing a weakly nonlinear velocity closure, assuming that the large-scale overturning circulation will become insensitive to the large-scale meridional density gradient when perturbation is large. In addition, self-sustained oscillation can also be realized in a one-dimensional Howard–Malkus loop model (Welander 1986), when considering temperature–salinity advection.

In this paper, we demonstrate that a combination of salinity advection and "enhanced mixing" can lead to a self-sustained multicentennial oscillation in a 4-box model. The enhanced mixing mechanism is parameterized in our box model, which is based on the results from a coupled model control run. We show that in a coupled model, the diffusion or mixing in the subpolar Atlantic can be enhanced due to the weak stratification when the AMOC is strong, or due to the active mesoscale and submesoscale eddies when the AMOC is weak. The enhanced mixing can restrain the positive salinity advection feedback, which can eventually lead to a self-sustained stable oscillation. Linear stability analyses further reveal that the oscillation period is determined by the eigenvalue of the system, which is controlled by the turnover time of the upper ocean. Without the enhanced mixing, the AMOC in the 4-box model is unsteady, exhibiting an oscillation with either growing or decaying amplitude.

This work differs from previous studies in the following aspects. First, only salinity equations are employed in our model for simplicity, and density perturbation is linearly determined by salinity perturbation. Second, we focus on the multicentennial time scale, different from the decadal to centennial time scales in RT97 and millennial time scale in Colin de Verdière et al. (2006). Third, only small oscillation of the AMOC around its stable equilibrium state is studied, and the step- or delta-function-like oscillations (Huang 1994; Sakai and Peltier 1999; Zhang et al. 2002; Sévellec and Fedorov 2014) are not our concern. The latter is more related to the climate regime shift.

The paper is organized as follows. In section 2, the multicentennial oscillation of the AMOC from a coupled model control run is analyzed briefly. In section 3, the 4-box model is introduced, and eigenvalues of the linear system are obtained. In section 4, enhanced mixing is parameterized in the salinity equation, based on the coupled model results presented in section 2. A self-sustained oscillation in the box model is exhibited, and its existence is explained theoretically. In section 5, effects of model geometry, external stochastic forcing, and nonlinear salinity advection on the multicentennial variability are discussed, followed by a summary in section 6.

2. Multicentennial oscillation in CESM

In this section, we investigate the low-frequency variability of the AMOC in a coupled climate model. Temporal evolutions of vertical temperature, salinity, and density structures in the North Atlantic are examined. Salinity diffusion and mixing are calculated. Analyses of the coupled model results provide the rationale for the assumptions used in the simple box model in section 3.

A long simulation was carried out using the Community Earth System Model (CESM, version 1.0) of the National Centre for Atmospheric Research (NCAR). The ocean horizontal grid has a uniform 1.125° spacing in the zonal direction, and nonuniform spacing in the meridional direction, whose resolution is 0.27° near the equator, extending to the maximum 0.65° at 60°N/S and then shrinking gradually to the poles. Detailed description can be found in Yang et al. (2015). The control run starts from the rest with the standard configuration for the preindustrial condition, and is integrated for 2500 years. The outputs during the last 1500 years are used

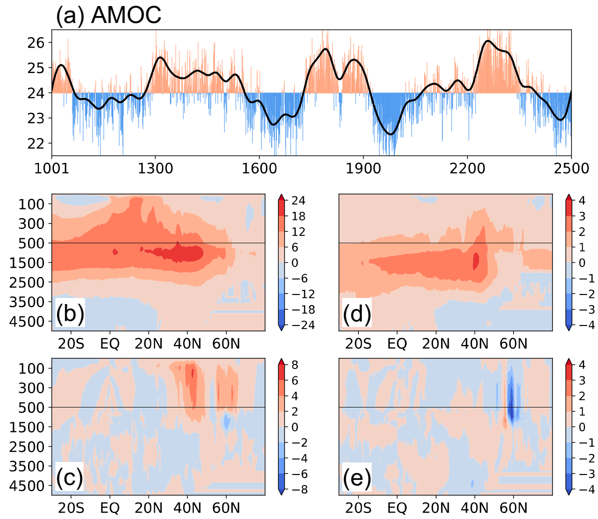

FIG. 1. (a) Atlantic meridional overturning circulation (AMOC) index (units: Sv; 1 Sv ≡ 10^6 m^3 s^{-1}). Thin vertical color bars show the annual mean AMOC with respect to its climatological mean of 24 Sv. The thick black curve is the low-pass-filtered AMOC index after applying a Lanczos filter with 121 weights, with a cutoff period of 60 years. The AMOC index is defined as the maximum streamfunction in the region of 20°–70°N between 200 and 3000 m in the Atlantic. (b),(c) Climatological patterns of Eulerian-mean and eddy-induced AMOC (units: Sv), respectively. (d),(e) Regression patterns of Eulerian-mean and eddy-induced AMOC, respectively, with respect to the mean-normalized filtered AMOC index.

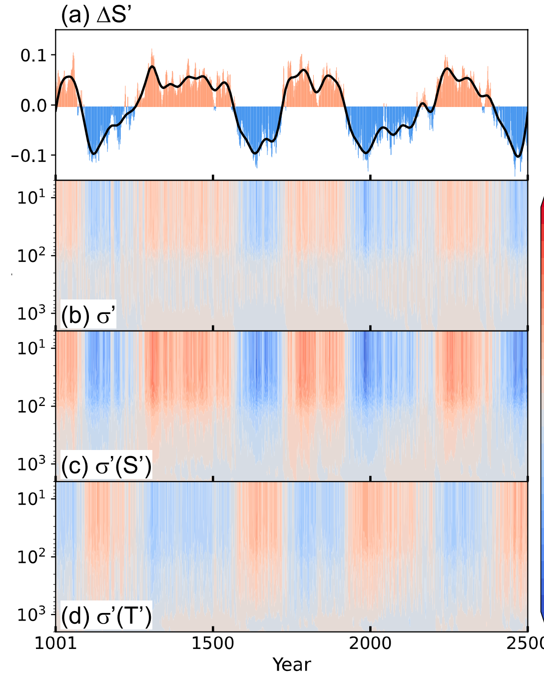

FIG. 2. (a) Time series of anomalous vertical salinity gradient between subpolar upper ocean (above 1000 m) and deeper ocean (units: psu). Thin vertical color bars show the annual mean anomalies. The thick black curve is the low-pass-filtered anomalies after applying a Lanczos filter with 121 weights, with a cutoff period of 60 years. Temporal evolutions of (b) annual mean anomalous potential density and the contributions due to (c) salinity change and (d) temperature change (units: kg m^{-3}). These variables are horizontally averaged over the subpolar Atlantic region defined in Fig. 3d.

for analysis. In the CESM, the velocity can be divided into Eulerian-mean and eddy-induced components; the latter consists of bolus velocity and submesoscale velocity (Gent and McWilliams 1990; Fox-Kemper and Ferrari 2008; Fox-Kemper et al. 2008, 2011). Each velocity component has its corresponding mass transport (i.e., streamfunction).

A multicentennial oscillation of the AMOC is identified in the CESM control run. Figure 1 shows the AMOC index and its spatial pattern. The AMOC index is defined as the maximum of the residual streamfunction in the region of 20°–70°N between 200 and 3000 m in the Atlantic. The low-pass filtered AMOC index exhibits clearly a multicentennial oscillation with a period between 300 and 400 years (Fig. 1a). The climatological mean of the total AMOC is about 24 Sv (1 Sv ≡ 10^6 m^3 s^{-1}), and the low-frequency variation is about 10% of the mean value. Figures 1b and 1c show the climatological mean patterns of Eulerian-mean AMOC and eddy-induced AMOC, respectively. The Eulerian-mean AMOC has the maximum strength of about 24 Sv around 40°N at the depth of ~1000 m. The eddy-induced AMOC has the maximum strength of about 8 Sv between 35° and 70°N at a shallower depth of 100–500 m, corresponding to the North Atlantic Deep Water formation region with strong meridional density gradient and deep convection (Yang et al. 2015).

The low-frequency Eulerian-mean AMOC shows a meridional coherent change in the whole Atlantic basin (Fig. 1d). The low-frequency eddy-induced AMOC, however, has remarkable change only locally in the subpolar Atlantic (Fig. 1e), revealed by their regression patterns on the mean-normalized AMOC index. Furthermore, the change in eddy-induced AMOC has a comparable magnitude but opposite sign in the subpolar deep convection region to the change in Eulerian-mean AMOC. This implies that a strong AMOC is concomitant with weakened eddy-induced AMOC; or when the AMOC is weak, the eddy-induced mixing is strong. Although the causality between the mean and eddy-induced AMOC is still unclear, Fig. 1 provides a clue that the eddy-induced transport may play a role in the multicentennial AMOC oscillation.

At the multicentennial time scale, the change in upper-ocean density in the subpolar Atlantic (Fig. 2b) is determined predominantly by the change in salinity (Fig. 2c), while temperature change (Fig. 2d) acts against density change. When the AMOC is strong (weak) (Fig. 1a), the density stratification is weak (strong) (Fig. 2b), which is mainly due to a more saline (fresh) upper ocean (Fig. 2c), suggesting a well (weakly) ventilated structure in the subpolar upper ocean. Lag–lead correlation analyses reveal that the surface density, salinity, and temperature changes in the subpolar Atlantic all lead the AMOC change by about 10 years (figure not shown). This suggests a positive salinity feedback in triggering AMOC change, while the temperature change has a slight damping effect at the same time.

The evolution of the anomalous salinity gradient (Fig. 2a, expressed as $\Delta S'$) between the subpolar upper ocean (above 1000 m) and deeper ocean resembles well the AMOC variation (Fig. 1a, expressed as q'); the former leads the latter by about five years. It is straightforward that there is a linear relationship between them (i.e., $q' \sim \Delta S'$). Both eddy-induced mixing and diffusion can change $\Delta S'$ in the subpolar ocean, and thus may have important influence on q'. These two processes are different: the eddy-induced mixing is related to mesoscale and submesoscale eddies at a relatively shallower depth and limited region as illustrated in Fig. 1e, while salinity diffusion is of molecular to turbulent scales, which occur over a broader horizontal and vertical region. Hereafter, we will use "salinity mixing" for simplicity, instead of "salinity diffusion and eddy-induced mixing."

To unravel the relationship between salinity mixing and $\Delta S'$ (equivalently, q'), scattering plots between them are shown in Fig. 3. Figure 3a suggests that the anomalous salinity in the subpolar upper ocean is damped more effectively when $\Delta S'$ is large. That is, when $\Delta S'$ is positively (negatively) large, the salinity mixing is negatively (positively) large so that the upper ocean saline (fresh) water can be removed efficiently. This nonlinear feature is mainly caused by the vertical salinity mixing when the AMOC is strong (i.e., $\Delta S' > 0$, $q' > 0$) (Fig. 3c) and by both the horizontal and vertical salinity mixing when the AMOC is weak (i.e., $\Delta S' < 0$, $q' < 0$) (Fig. 3b). This nonlinear feature can be physically understood as follows. When the stratification in the subpolar ocean is weak and the AMOC is strong, upper-ocean salinity anomaly can be mixed into the deeper ocean more efficiently by salinity diffusion. When the stratification in the subpolar ocean is strong and the AMOC is weak, the salinity diffusion is weak but the eddy-induced salinity mixing can enhance the downward mixing. Instead of canceling each other completely, the combined effect of diffusion and eddy-induced mixing is that the salinity mixing is always enhanced when the AMOC anomaly is large. From now on, we simply use "enhanced mixing" to mean "enhanced eddy-induced mixing or diffusion when the AMOC anomaly is large."

Here, the salinity mixing is obtained based on the following equation:

$$V\frac{\partial S'}{\partial t} = F_{\text{surf}} + F_{\text{Euler}} + F_{\text{mixing}}, \tag{1}$$

where S' is salinity anomaly; F_{surf} and F_{Euler} represent the surface freshwater effect and Eulerian-mean advection effect, respectively; and F_{mixing} includes both horizontal and vertical mixing and both eddy-induced mixing and diffusion. Also, V is the total volume of the subpolar ocean above 1000 m in depth, with the horizontal range outlined in Fig. 3d; $V\partial S'/\partial t$, F_{surf}, and F_{Euler} (units: psu Sv^{-1}) can be calculated accurately offline based on model outputs. Therefore, F_{mixing} is obtained as the residual of these three terms, which is more reliable than directly calculating the

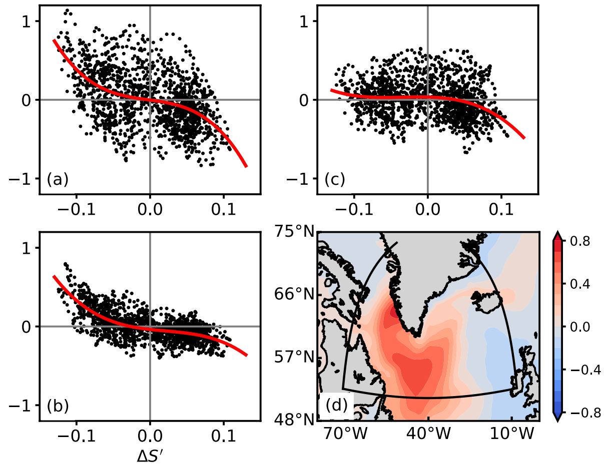

FIG. 3. (a) Scattering plots of anomalous salinity mixing (units: psu Sv^{-1}; ordinate) in the subpolar upper ocean (above 1000 m) vs the salinity difference anomaly (abscissa) between subpolar upper ocean and deeper ocean (units: psu). (b),(c) The horizontal and vertical components (units: psu Sv^{-1}), respectively. The red curve shows the cubic regression result, and all these data are filtered with a cutoff period of 10 years. (d) Sea surface density anomaly (units: kg m^{-3}) regressed onto the mean-normalized filtered AMOC index. Black curves encircle the region defined for the area-average region, and these curves are parallel to the grid lines of the ocean model. In (a), the expression for cubic regression $F_{\text{mixing}} = -285.15 \times (\Delta S')^3 - 2.51 \times (\Delta S')^2 - 1.28 \times (\Delta S') - 0.003$, and the explained variance is about 25%; the effective rank for the scaled Vandermonde coefficient matrix is 4, suggesting the cubic regression polynomial is significant.

mixing effect. In addition, we calculate directly the horizontal mixing. The vertical mixing is obtained as the residual of the total F_{mixing} and the horizontal component. Note that the way to decompose F_{mixing} into horizontal and vertical components is not accurate, but the total F_{mixing} is reliable. We need to bear in mind that large uncertainty exists in simulated eddies in ocean models, so the eddy-induced effect may vary among different models. Results here are meant to show the enhanced mixing mechanism may exist in coupled models.

Finally, based on the cubic regression between salinity mixing and $\Delta S'$ (red curve in Fig. 3a) and considering the linear relationship between $\Delta S'$ and q', the enhanced mixing effect can be expressed as follows:

$$F_{\text{mixing}} \sim -(\Delta S')^3 \sim -(q')^2\Delta S' \sim -k_m \Delta S', \tag{2}$$

where $k_m \sim (q')^2$, parameterizing the enhanced mixing effect when the AMOC is large. Here, we emphasize that the detailed forms of Eq. (2) and k_m are not important. The regression between salinity mixing and $\Delta S'$ can be linear or even the power of 5. The cubic relationship is just a reasonable outcome from the coupled model we used in this work. In summary, the enhanced mixing mechanism will be used in the box model in section 4.

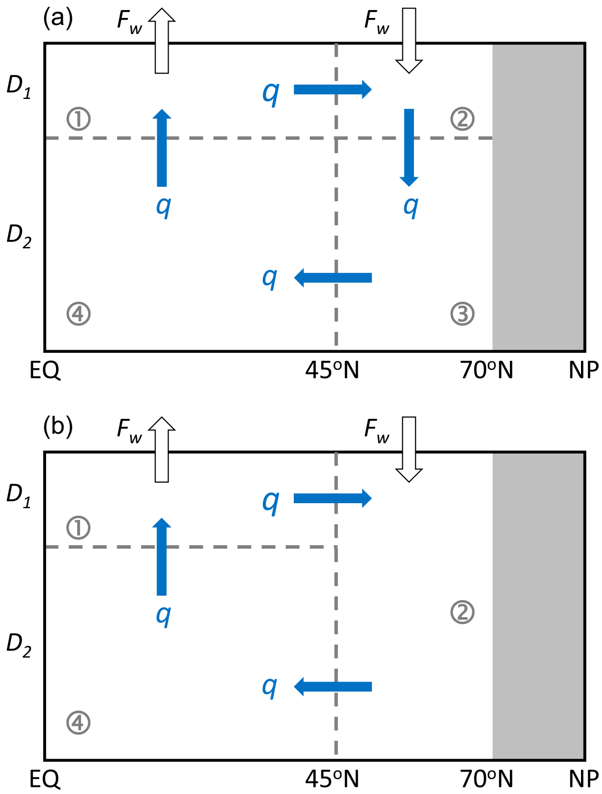

FIG. 4. Schematic diagrams of box models: (a) 4-box ocean model and (b) 3-box ocean model. Ocean boxes are denoted by ①, ②, ③, and ④. Boxes 1 and 4 represent the upper and lower layers of the tropical ocean, respectively; and boxes 2 and 3 represent the upper and lower layers of the subpolar ocean, respectively. D_1 and D_2 are the depths of upper and lower ocean layers, respectively; F_w is the net freshwater gain (loss) in the subpolar (tropical) ocean; q represents the thermohaline circulation. With the extreme vertical mixing in the subpolar ocean, the 4-box model in (a) can be interpreted as a 3-box model in (b).

3. Hemispheric box model

The conceptual model used here consists of four ocean boxes (Fig. 4a). With a zonal width of 60°, the meridional scales of these boxes are 45° and 25° for the tropical and subpolar basins, respectively. This selection is based on the horizontal patterns of surface density variances from the CESM results (Fig. 3d). The AMOC is included explicitly, with sinking in the extratropics and rising in the tropics. Such box model was first presented in Stommel (1961), and has been used in different forms by many researchers (e.g., Marotzke 1990; Huang et al. 1992; Nakamura et al. 1994; Tziperman et al. 1994; Marotzke and Stone 1995; Yang et al. 2016; Zhao et al. 2016). Since the relaxation time for temperature is substantially shorter than that for salinity (Huang 1994), the salinity effect provides the main control on low-frequency variation of density in the subpolar ocean (Rooth 1982), which is confirmed by our CESM control run (Fig. 2). Therefore, only salinity changes are considered in the box model. The salinity equations for the 4-box ocean model are written as follows:

$$V_1\dot{S}_1 = q(S_4 - S_1) + F_w, \tag{3a}$$

$$V_2\dot{S}_2 = q(S_1 - S_2) - F_w, \tag{3b}$$

$$V_3\dot{S}_3 = q(S_2 - S_3), \tag{3c}$$

$$V_4\dot{S}_4 = q(S_3 - S_4), \tag{3d}$$

where V_i ($i = 1, 2, 3, 4$) is the volume of each box, q is the volume transport by the AMOC, and F_w is freshwater flux. The equilibrium state of the box model is

$$\overline{q}(\overline{S}_1 - \overline{S}_2) = \overline{F}_w, \quad \overline{S}_2 = \overline{S}_3 = \overline{S}_4. \tag{4}$$

Here, $\overline{q}$ is given by a constant of 10 Sv in the box model, which is a typical value in previous single hemispheric studies (Winton and Sarachik 1993; Cessi 1994; Roebber 1995). The upper ocean in the box model is 500 m in thickness, so that the turnover time in the upper ocean is similar to that in the CESM. Based on the CESM results, $\overline{S}_1$ and $\overline{S}_2$ are set to 36 and 33.5 psu, respectively, which gives $\overline{F}_w = 2.5 \times 10^7$ psu m^3 s^{-1}. Please refer to Table 1 for other parameters.

We assume a small amplitude of oscillation with respect to the equilibrium climate, and do not consider surface freshwater flux change (i.e., $F_w = \overline{F}_w$). The total volume transport q consists of a mean state $\overline{q}$ and salinity-driven perturbation q'. The latter is assumed to be linearly proportional to meridional density difference caused only by salinity change:

TABLE 1. Parameters used in this study.

Symbol	Physical meaning	Value
V_2	Volume of upper subpolar Atlantic box	2.8×10^{15} m^3
V_1, V_3, V_4	Volumes of upper tropical Atlantic, lower subpolar Atlantic, and lower tropical Atlantic boxes, respectively	$5V_2$, $7V_2$, $35V_2$
D_1, D_2, D	Depths of upper box, lower box, and total, respectively	500, 3500, 4000 m
$\overline{S_1}$, $\overline{S_2}$, $\overline{S_3}$, $\overline{S_4}$	Reference salinity values of the four ocean boxes	36, 33.5, 33.5, 33.5 psu
$\overline{q}$	Equilibrium AMOC strength	10 Sv (10^6 m^3 s^{-1})
F_w	Total virtual salt flux	2.50×10^7 psu m^3 s^{-1}
β	Haline contraction coefficient	7.61×10^{-4} psu^{-1}
ρ_0	Reference density	1.00×10^3 kg m^{-3}
λ	Linear closure coefficient	12 Sv kg^{-1} m^{-3}

$$q = \overline{q} + q' = \overline{q} + \lambda \Delta\rho', \tag{5}$$

where

$$\Delta\rho' = \rho_0 \beta[\delta(S_2' - S_1') + (1 - \delta)(S_3' - S_4')] \quad \text{and}$$
$$\delta = \frac{V_1}{V_1 + V_4} = \frac{V_2}{V_2 + V_3} = \frac{D_1}{D}. \tag{6}$$

Here, λ is a linear closure parameter, depicting the efficiency that the meridional perturbation salinity gradient affects the AMOC; ρ_0 is the reference seawater density; β is the saline expansion coefficient of seawater; D_1 and D are upper-level and total ocean depths, respectively. Their values are listed in Table 1. The system of Eqs. (3)–(6) is similar to that of RT97, except that the subpolar box is divided into two boxes (Fig. 4a), for further consideration of vertical mixing in the subpolar ocean. In addition, while temperature is not explicitly shown in the equations, it virtually determines the mean transport $\overline{q}$ and freshwater flux $\overline{F}_w$, which have indirect impacts on the eigenmodes of the system.

The linearized version of Eq. (3) can be written as follows:

$$V_1 \dot{S}_1' = q'(\overline{S_4} - \overline{S_1}) + \overline{q}(S_4' - S_1'), \tag{7a}$$

$$V_2 \dot{S}_2' = q'(\overline{S_1} - \overline{S_2}) + \overline{q}(S_1' - S_2'), \tag{7b}$$

$$V_3 \dot{S}_3' = \overline{q}(S_2' - S_3'), \tag{7c}$$

$$V_4 \dot{S}_4' = \overline{q}(S_3' - S_4'), \tag{7d}$$

where S_i' ($i = 1, 2, 3, 4$) is the perturbation salinity of each ocean box.

Eigenvalues can be calculated numerically from the linearized Eq. (7). With parameters in Table 1, there are a pair of conjugate eigenvalues $[0.31 \pm 5.83i] \times 10^{-10}\ \mathrm{s^{-1}}$, corresponding to a 340-yr period and 1025-yr e-folding time. This is a marginally unstable mode because of the small positive real part. The eigenvector $[S_1', S_2', S_3', S_4']$ is $[-0.11 + 0.74i, 0.55 - 0.08i, 0.20 - 0.29i, -0.04 - 0.04i]$, showing a dipole pattern between the tropical and subpolar upper oceans by either the real part or the imaginary part. The other two eigenvalues are 0 and $-37.4 \times 10^{-10}\ \mathrm{s^{-1}}$, respectively, suggesting a zero mode (caused by the total salt conservation) and a purely damped mode with e-folding time of about 8.5 years.

4. Self-sustained oscillation in the box model

a. Unstable oscillation

Results from forward numerical integration of Eq. (7) are shown in Fig. 5. The fourth-order Runge–Kutta method is used to solve Eq. (7), with an initial perturbation of $S_2' = -0.02$ psu and $S_1' = S_3' = S_4' = 0$. The integration time step is 7.2 days, and the total integration length is 10000 years. Given the velocity closure parameter $\lambda = 12\ \mathrm{Sv\ m^{-3}\ kg^{-1}}$, the time series of salinity anomalies show a periodic oscillation of about 340 years, and a gradually enhanced amplitude (Fig. 5a), which are exactly predicted by the eigenvalue discussion in section 3. The term S_1' leads S_2' by about $2\pi/3$, suggesting roughly a dipole pattern in tropical–subpolar surface salinity distribution. Note that S_2' only leads S_3' slightly, suggesting an efficient vertical advection by the mean AMOC. The perturbed AMOC (q') shows a similar oscillation, with its amplitude growing gradually (Fig. 5b). The term q' lags S_1' by about $2\pi/3$, and is roughly out of phase with $(S_1' - S_2')$. Besides, q' lags $(S_2' - S_3')$ by about $\pi/2$. This phase lag can be reduced by including vertical mixing between the two subpolar boxes with a constant mixing coefficient. Note that the integral of $d(S_2')^2/dt$ in a period is positively correlated to the growth rate. To identify the mechanism for amplitude change, the three terms in Eq. (7b) are multiplied by S_2' and shown in Fig. 5c. We can see the growing perturbation comes from the positive perturbation advection feedback $[q'(\overline{S_1} - \overline{S_2})]$, and the negative mean advection feedback $[\overline{q}(S_1' - S_2')]$ tends to restrain the growth, which is consistent with the results in Marotzke (1996).

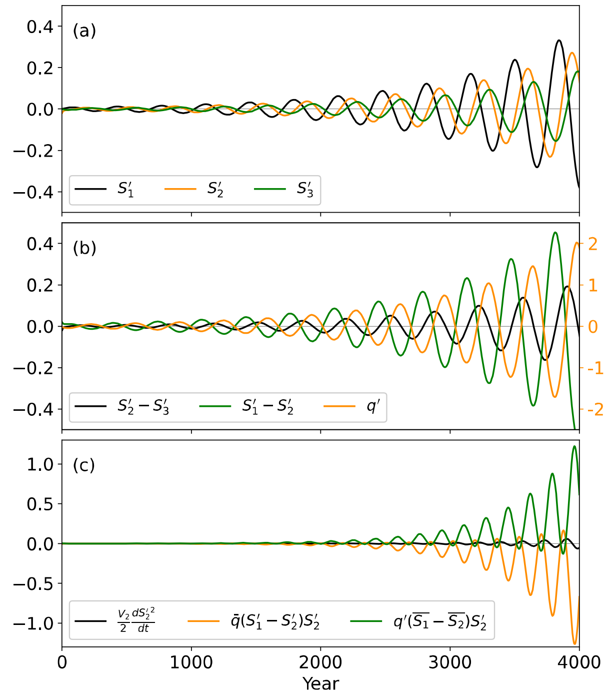

FIG. 5. Unstable oscillation in the 4-box model without the enhanced vertical mixing considered in the subpolar ocean. (a) Salinity anomalies S_1', S_2', and S_3' (units: psu); (b) salinity stratification in the subpolar ocean $(S_2' - S_3')$ (units: psu), the meridional salinity gradient $(S_1' - S_2')$ (units: psu), and AMOC anomaly (q') (units: Sv). The vertical coordinate on the right side is for q'. (c) The terms in Eq. (7b), which are multiplied by S_2' to represent the evolution of amplitude change (units: $\mathrm{psu^2\ Sv^{-1}}$). The linear closure parameter $\lambda = 12\ \mathrm{Sv\ kg^{-1}\ m^{-3}}$, and its nondimensional value $M = 0.285$.

b. Self-sustained oscillation with enhanced mixing

In this subsection, we show that including the enhanced mixing process in the subpolar ocean leads to a stable self-sustained oscillation. Terms representing the enhanced vertical mixing in the subpolar ocean are added to Eqs. (7b) and (7c) as follows:

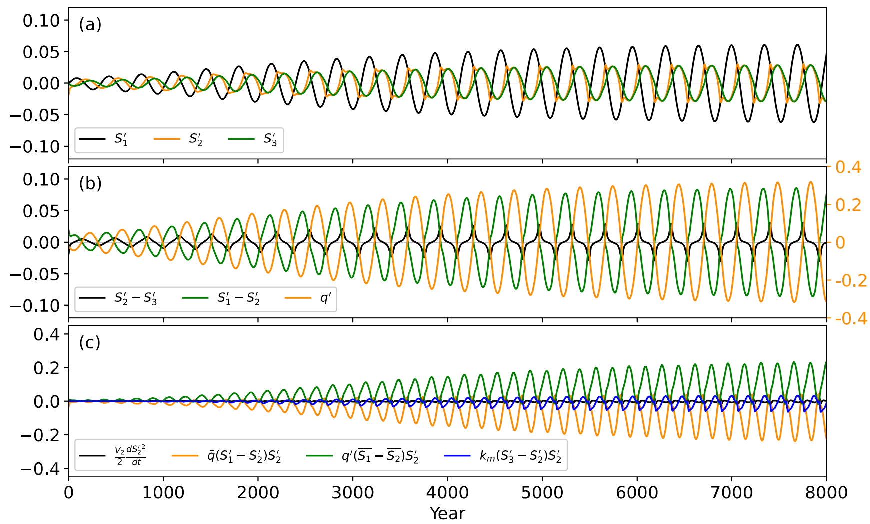

FIG. 6. As in Fig. 5, but for self-sustained oscillations when considering the enhanced vertical mixing in the subpolar ocean. In (c), the units are 10^{-1} psu^2 Sv^{-1}.

$$V_2\dot{S}_2' = q'(\overline{S_1} - \overline{S_2}) + \overline{q}(S_1' - S_2') - k_m(S_2' - S_3'), \tag{8a}$$

$$V_3\dot{S}_3' = \overline{q}(S_2' - S_3') + k_m(S_2' - S_3'), \tag{8b}$$

where k_m (units: m^3 s^{-1}) is proportional to vertical mixing coefficient. In this paper, k_m is defined as a function of the overturning rate anomaly squared:

$$k_m = \kappa q'^2. \tag{9}$$

Here, κ is a positive constant (units: m^{-3} s), so that vertical mixing in the subpolar ocean is always enhanced when perturbation grows. Specifically, we choose $\kappa = 10^{-3}$ m^{-3} s.

We would like to emphasize several points here. First, the oscillation behaviors are similar for different forms of k_m, as long as the enhanced mixing mechanism can be explicitly expressed. For example, we can also define $k_m = 100|q'|$. Second, the value of κ affects the amplitude of the oscillation but not the period. Third, a background vertical mixing can be included, say, $k_m = \overline{k}_m + k_m'$, which will not qualitatively change the results as long as $\overline{k}_m$ is not too big. The background vertical mixing is neglected for simplicity, although using a nonzero $\overline{k}_m$ may give more realistic results. Fourth, while only vertical mixing is included in the box model, horizontal mixing is also important for the enhanced mixing mechanism as revealed in the CESM results (Fig. 3b).

A speedup of the AMOC can lead to an increase of S_2'. This would increase the subpolar upper-ocean density and reduce stratification, enhancing downward diffusion, which in turn helps remove upper-ocean saline water. A slowdown of the AMOC can lead to a fresher subpolar upper ocean. While the stratification becomes more stable, the vertical mixing can become stronger due to eddies' effect, as examined in section 2. The enhanced eddy activities help mix the anomalous freshening signal in the upper ocean downward, so the signal can flow out of the subpolar faster. A self-sustained oscillation of the system exists under this mechanism (Fig. 6). Now, the growing perturbation due to the positive perturbation advection feedback $[q'(\overline{S_1} - \overline{S_2})]$ can be eventually balanced by the combined negative feedback of mean advection $[\overline{q}(S_1' - S_2')]$ and enhanced vertical mixing $[k_m(S_3' - S_2')]$ (Fig. 6c). The latter provides a critical mechanism to stabilize the system.

c. Understanding the self-sustained oscillation

The enhanced mixing helps stabilize the system by removing the subpolar surface salinity anomaly out of the region. To further understand the self-sustained oscillation, let us assume an extreme situation: the vertical mixing is so strong that the salinity in the subpolar upper ocean and that in the subpolar lower ocean almost instantly becomes the same. Therefore, the 4-box model (Fig. 4a) can be interpreted as a 3-box model (Fig. 4b), making it comparable to that of RT97. Now, Eqs. (7) and (8) become

$$V_1\dot{S}_1' = q'(\overline{S_4} - \overline{S_1}) + \overline{q}(S_4' - S_1'), \tag{10a}$$

$$V_2\dot{S}_2' = q'(\overline{S_1} - \overline{S_2}) + \overline{q}(S_1' - S_2'), \tag{10b}$$

$$V_4\dot{S}_4' = \overline{q}(S_2' - S_4'), \tag{10c}$$

where

$$q' = \lambda\Delta\rho' = \lambda\rho_0\beta[S_2' - \delta S_1' - (1 - \delta)S_4')] \quad \text{and}$$
$$\delta = \frac{V_1}{V_1 + V_4} = \frac{D_1}{D}. \tag{11}$$

The 3-box model has the same equilibrium as the 4-box model. By applying the total salt conservation ($V_1S_1' + V_2S_2' + V_4S_4' =$ constant), the 3-box system can be further simplified, and its eigenvalues can be obtained theoretically. Here, we define the following quantities:

$$S_d \equiv \frac{\overline{F}_w}{\overline{q}} = \overline{S_1} - \overline{S_4} = \overline{S_1} - \overline{S_2}; \quad \rho_d = \delta\beta\rho_0 S_d$$

$$T_n = \frac{V_1 + V_2 + V_4}{\overline{q}}; \quad \delta_i = \frac{V_i}{V_1 + V_2 + V_4}, \quad i = 1,\ 2,\ 4$$

$$\tau = \frac{t}{T_n}; \quad a' = \frac{S_1' - S_2'}{S_d}; \quad h' = \frac{\Delta\rho'}{\rho_d}; \quad M = \frac{\rho_d}{\overline{q}}\lambda.$$

Equation (10) can be reduced to

$$\frac{da'}{d\tau} = -C_3 a' - (C_4 + C_1 M)h', \tag{12a}$$

$$\frac{dh'}{d\tau} = C_2 a' + C_2 M h'. \tag{12b}$$

Assuming the form of solution $a' = Ae^{\omega\tau}$, Eq. (12) has an eigenvalue:

$$\omega = \frac{1}{2}[(C_2 M - C_3) \pm \sqrt{(C_2 M - C_3)^2 - 4C_2 C_4(1 - M)}], \tag{13}$$

where $C_1 = 1/\delta_1 + 1/\delta_2$, $C_2 = 1/(\delta_1\delta_2)$, $C_3 = 1/\delta_1 + 1/\delta_2 + 1/\delta_4$, and $C_4 = 1/\delta_4$.

Based on (13), the essential stability condition for the system is

$$M \le \min\left(\frac{C_3}{C_2}, 1\right) \tag{14}$$

and the oscillation condition of the system is

$$M_1 < M < \min(M_2, 1), \tag{15}$$

where M is the nondimensional linear closure parameter, and

$$M_1 = \frac{C_3 - 2C_4}{C_2} - \frac{2}{C_2}\sqrt{C_4^2 + C_4(C_2 - C_3)},$$

$$M_2 = \frac{C_3 - 2C_4}{C_2} + \frac{2}{C_2}\sqrt{C_4^2 + C_4(C_2 - C_3)}.$$

Therefore, $\lambda_{1,2} = (\overline{q}/\rho_d)M_{1,2}$.

Figure 7 shows the dependence of real and imaginary parts of ω on the nondimensional parameter M. Given the parameters listed in Table 1, $M_1 \approx -0.02$ and $M_2 \approx 0.51$. When $M > M_2$ or $M < M_1$, there are only two real positive or negative ω (Fig. 7a), suggesting the system has only exponentially growing (decaying) modes. An oscillatory mode occurs when $M_1 < M < M_2$. With the decrease of M, the oscillation mode changes from an unstable oscillation [Re $(\omega) > 0$] to a stable oscillation [Re $(\omega) < 0$] (Fig. 7b). When $M = 0$, $q' = 0$; that is, the AMOC does not respond to any salinity change, and the oscillation mode is a strong damped mode, with an oscillation time scale of about 1000 years and damping time scale of about 50 years. The peak value of the imaginary part of ω corresponds to the shortest time scale (Fig. 7b), which is about 350 years $[2\pi(V_1V_2)^{1/2}/\overline{q}]$ with a damping time scale of 340 years when $M \approx 0.245$.

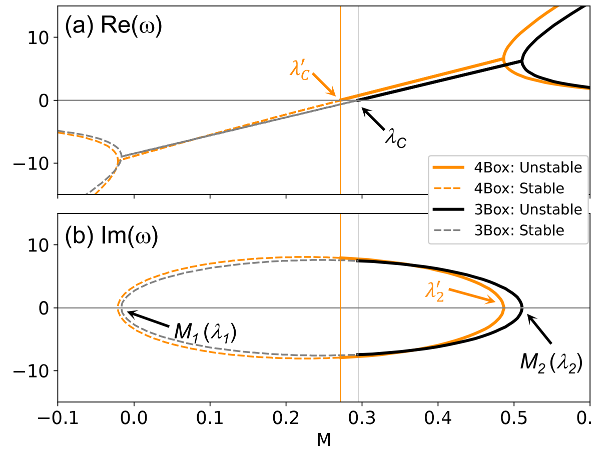

FIG. 7. Dependence of eigenvalue ω in the 3-box and 4-box models on the nondimensional linear closure parameter M, for the (a) real and (b) imaginary parts of the nondimensional eigenvalue ω. Black curves are for the 3-box model, which are obtained theoretically. Orange curves are for the 4-box model without the enhanced vertical mixing, which are obtained numerically. The terms λ_1, λ_2, and λ_C are dimensional values of M for the 3-box model, and λ_2' and λ_C' are for the 4-box model; $\lambda_C' = 11.45$ and $\lambda_C = 12.42$ Sv kg^{-1}m^{-3}, and the corresponding $M = 0.272$ and 0.295, respectively.

Given an eigenvalue ω, the corresponding eigenvector is $[\omega/C_2 - M, 1]^{\mathrm{T}} \equiv [p, 1]^{\mathrm{T}}$. When ignoring the term $e^{\omega\tau}$, the theoretical solutions to S_i' and q' can be written as follows:

$$S_1' = S_d p + S_2', \quad S_2' = \delta_1 S_d, \quad S_4' = \frac{\delta}{\delta - 1}S_d(1 + p) + S_2', \tag{16}$$

$$q' = \lambda\delta\beta\rho_0 S_d = \overline{q}M. \tag{17}$$

Therefore, based on Eqs. (10b), (16), and (17), the salinity tendency in the subpolar box is

$$V_2\dot{S}_2' \sim (q' S_d + \overline{q}S_d p) = \overline{q}S_d(M + p), \tag{18}$$

whose sign is determined by Re$[M + p]$. Here, the salinity tendency caused by perturbation flow tends to have the same sign as the salinity anomaly (here $M > 0$ in most cases, as shown in Fig. 7b). The salinity tendency caused by mean flow relies on p, which can be of opposite sign when Re$[\omega] < C_2 M$. Further, if Re$[\omega] < 0$, we have Re$[p] < -M$; therefore, the negative feedback by the mean flow would dominate over the positive feedback by the perturbation flow, and the 3-box model is stable. In summary, the perturbation advection of mean salinity has a positive feedback, and the mean advection of salinity anomaly has a negative effect. A self-sustained oscillation can be realized when these two feedbacks are balanced.

Mathematically, a stable oscillation in the 3-box model can exist when Re$[\omega] < 0$. Therefore, the stability condition can be expressed in dimensional form as follows:

$$\lambda < \lambda_C \equiv \frac{\overline{q}^2}{\rho_0 \beta \overline{F}_w}\left[1 + \frac{\delta_2}{\delta(1-\delta)}\right], \tag{19}$$

where λ_C (marked in Fig. 7a) is the critical linear closure parameter when $\mathrm{Re}[\omega] = 0$, which is determined by mean AMOC strength $\overline{q}$, surface freshwater flux $\overline{F}_w$ as well as basin geometry. Equation (19) shows that a stronger $\overline{F}_w$ and a weaker $\overline{q}$ give a smaller λ_C, implying higher possibility for an unstable oscillation, since the background meridional salinity gradient in this situation will be stronger. This is qualitatively consistent with previous studies showing that increasing freshwater flux could lead to a regime shift (e.g., Zhang et al. 2002). In addition, salinity anomalies also spend more time at the surface with a weaker mean AMOC. This will also make the system more unstable from a Lagrangian viewpoint, and this is why we have a quadratic term of $\overline{q}$. Overall, these are similar to the results of Sévellec et al. (2006), that is, a competition between the mean AMOC and freshwater flux determines the salinity behavior. Equation (19) also shows a bigger volume of the subpolar ocean (δ_2) gives a larger λ_C, implying a higher probability for a stable oscillation. In this situation, the salinity difference anomaly between subpolar and tropical upper oceans is larger under the same q', and thus the mean advection of salinity anomaly is stronger, which would result in a stronger stabilizing effect. This is consistent with the analysis on Eq. (18).

Linear stability analyses on the 4-box model [Eq. (7)] without the enhanced vertical mixing can be done numerically. The results are also plotted in Fig. 7 for comparison. Generally, the eigenvalues in the 3-box and 4-box models are very close to each other. However, there is a subtle but very important difference between them: The 3-box model is more stable than the 4-box model, and the critical linear closure parameter in the 4-box model, noted as λ'_C, is slightly smaller than λ_C in the 3-box model. A neutral oscillation can be observed in the 4-box model when $\lambda = \lambda'_C$ and in the 3-box model when $\lambda = \lambda_C$.

Figure 8 shows the oscillation behaviors of the AMOC in the 3-box model and 4-box model with and without the enhanced vertical mixing under different λ. When $\lambda < \lambda'_C$, the AMOC in all models exhibits a decaying oscillation (Fig. 8a). When $\lambda > \lambda_C$, the AMOC in all models shows an unstable oscillation with a fast-growing amplitude (Fig. 8c), which implies that even an extreme vertical mixing is still inadequate to restrain the growing perturbation. Here, we emphasize that a self-sustained oscillation can only exist in the 4-box model with the enhanced vertical mixing. The self-sustained oscillation is meant to be a growing oscillation due to the linear instability that can be constrained by itself as shown in Fig. 6. While neutral oscillations ($\mathrm{Re}[\omega] = 0$) can be found in the 3-box model and 4-box model without the enhanced vertical mixing, they cannot grow up from small perturbation.

A self-sustained oscillation can exist in the 4-box model with the enhanced vertical mixing when $\lambda'_C < \lambda < \lambda_C$. Within this parameter range, the 3-box system is stable, while the 4-box system without the enhanced vertical mixing is unstable (Fig. 7a). As we know from linear analyses that energy is

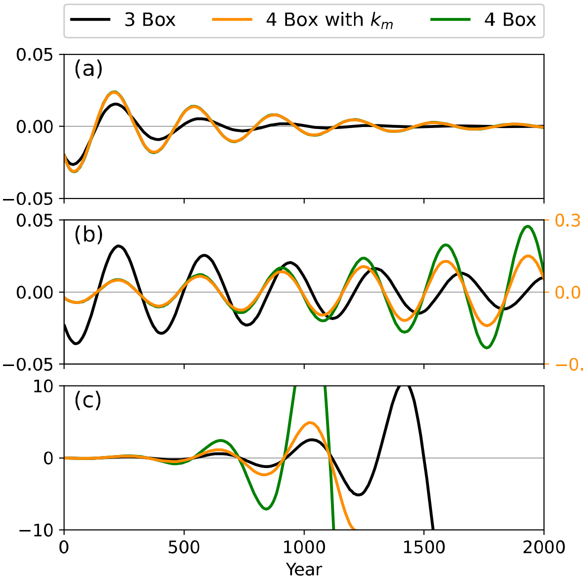

FIG. 8. Oscillations of AMOC anomalies (units: Sv) in the 3-box and 4-box models with and without the enhanced vertical mixing. (a) $M = 0.25$ ($\lambda < \lambda'_C$, region 1 in Fig. 9), showing decaying oscillations for both models. (b) $M = 0.285$ ($\lambda'_C < \lambda < \lambda_C$, region 2 in Fig. 9), showing a decaying oscillation in the 3-box model, a self-sustained oscillation 4-box model with k_m and a growing oscillation in the 4-box model without k_m. The vertical coordinate on the right side is for the 4-box model with k_m. (c) $M = 0.35$ ($\lambda > \lambda_C$, region 3 in Fig. 9), showing growing oscillations in both models. Both λ'_C and λ_C are marked in Fig. 7a.

provided by the mean salinity gradient in the upper ocean, salinity anomaly accumulates in the subpolar upper ocean and then flows downward and southward. When the AMOC is close to its mean state (i.e., $q' \sim 0$), the system is unstable because the enhanced mixing plays no role ($k_m \sim 0$) in the removal of salinity anomalies from the subpolar ocean. When the AMOC anomaly is large, the enhanced vertical mixing accelerates the outflow of salinity anomaly in the subpolar upper ocean. When the vertical mixing is too strong, salinity anomaly will be removed before it grows, and the system becomes stable again, similar to the 3-box model as the limit.

5. Discussion

a. *Oscillation dependence on model geometry*

Model geometry can affect both oscillation period and *e*-folding time of the system (Fig. 9). Under a reasonable range of the basin size, the multicentennial time scale is notable (Fig. 9a), since this time scale is fundamentally determined by the background parameters, such as the mean AMOC ($\overline{q}$) and the total volume of the upper ocean ($V_1 + V_2$). These two parameters suggest an upper-ocean turnover time $[(V_1 + V_2)/\overline{q}]$ of about 54 years, given the values listed in Table 1. This turnover time corresponds to an oscillation period of 340 years ($2\pi \times 54$), which is similar to the period of the eigenvalue through the linear stability analysis on

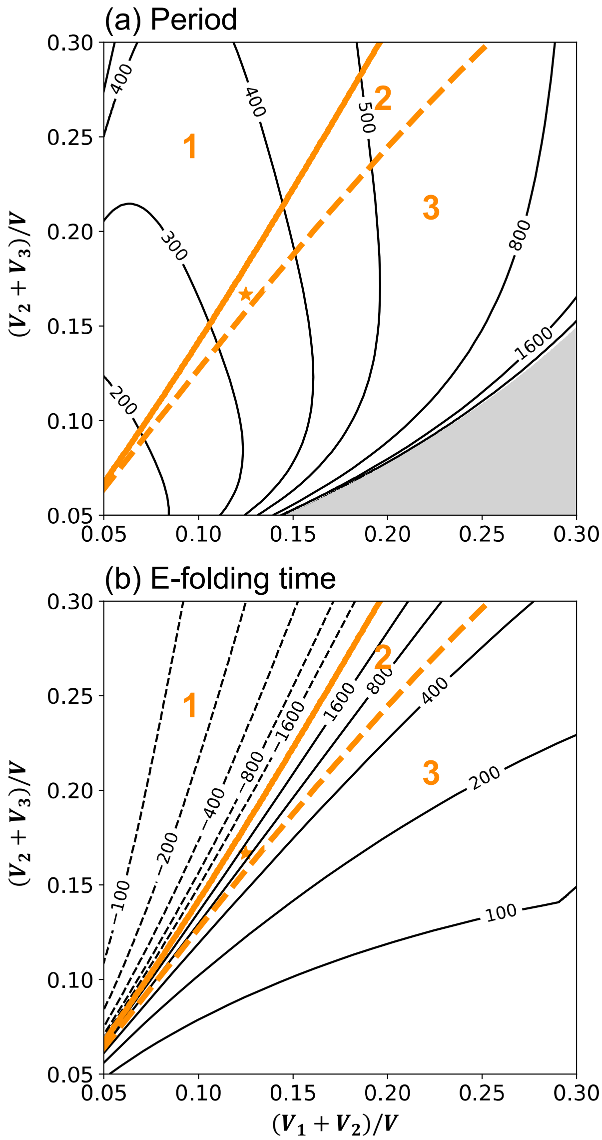

FIG. 9. Relations of the (a) period and (b) *e*-folding time of oscillation modes in the 4-box model without enhanced vertical mixing to the relative geometry of the ocean boxes (units: years). The abscissa and ordinate represent the volume fractions of upper ocean $(V_1 + V_2)/V$ and subpolar ocean $(V_2 + V_3)/V$, respectively, where V is the total ocean volume. The gray region in (a) denotes the region of no oscillation modes. Solid and dashed orange curves show the location of critical values λ'_C in the 4-box model and λ_C in the 3-box model, respectively. The oscillations are decayed in region 1, self-sustained in region 2, and unstable in region 3 when considering the enhanced vertical mixing. The star denotes the standard geometry and mode for parameters listed in Table 1.

Eq. (7) in section 3. The consistency between the turnover time of overturning circulation and the oscillation period of the system was revealed theoretically in Sévellec et al. (2006), in which analytical expressions for the oscillation period were derived for the fixed-temperature case and a more general case including both salinity and temperature changes.

The dependence of the 4-box eigenvalue on model geometry is illustrated in Fig. 9. Here, for simplicity and without losing generality, we keep the equilibrium $\overline{q}$, $\overline{F}_W$, the ocean total volume, and λ in Table 1 unchanged. Figure 9a shows that for a given upper-ocean volume $(V_1 + V_2)$, the oscillation period is weakly sensitive to the subpolar ocean volume $(V_2 + V_3)$; for a given subpolar ocean volume, the oscillation period increases monotonically with the increase of the upper-ocean volume. In other words, for a bigger upper-ocean volume, there would be a longer oscillation mode. Note that under a reasonable range of basin geometry, the millennium oscillation mode has a shorter positive *e*-folding time (Fig. 9b). This implies that the *intrinsic* millennium modes would have to be fast-growing modes in our hemispheric box model. Bear in mind that this conclusion is obtained based on the equilibrium $\overline{q}$ and $\overline{F}_W$ given in Table 1, and a more thorough study under different mean state of climate is needed.

The self-sustained oscillation can exist only in region 2, which is enclosed by the two orange lines in Fig. 9. This region denotes the regime where unstable oscillation occurs in the 4-box model while stable oscillation appears in the 3-box model, as discussed in section 4c. In region 1, the modes in both 3-box and 4-box models are decayed modes with negative *e*-folding time (Fig. 9b). In region 3, the modes in both 3-box and 4-box models are unstable, and even extreme mixing cannot lead to a stable oscillation. The orange star in Fig. 9 denotes the mode under the standard parameters in Table 1. The gray region in Fig. 9a denotes the region of no oscillation mode (i.e., the situation when $\lambda \geq \lambda'_2$). In general, under these ranges of parameters, a naturally self-sustained oscillation, relatively, is not that easy to happen, in terms of the ratio of region 2 to the total area. This might explain the fact that, in reality, relative to the other low-frequency climate variabilities, the multicentennial oscillation is under appreciated and inadequately studied (Stocker and Mysak 1992).

b. *Multicentennial oscillation forced by stochastic freshwater flux*

External stochastic forcing can also excite a multicentennial oscillation in the 4-box model (Fig. 10). We test the response of stable modes to stochastic forcing in the 4-box model. The linear closure parameter $\lambda = 9.45$ Sv m^{-3} kg^{-1}, corresponding to an eigenvalue with a period of 332 years and *e*-folding time of 285 years. This stable mode is within region 1 of Fig. 9. After adding a stochastic freshwater perturbation, Eq. (8a) of the 4-box model is rewritten as follows:

$$V_2\dot{S}'_2 = \cdots + V_2 N, \tag{20}$$

where N denotes the random freshwater perturbation, which is generated from a first-order autoregressive model:

$$N_{k+1} = \alpha N_k + \sigma G_k. \tag{21}$$

The noise N at time step $k + 1$ is generated from the noise at time step k and a standard Gaussian random variable G_k.

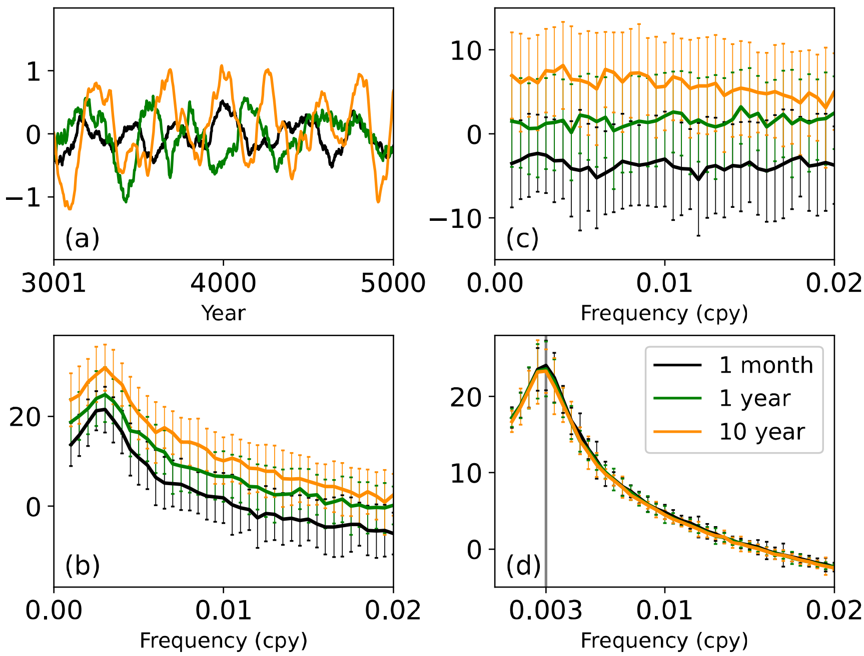

FIG. 10. (a) Time series of AMOC anomaly (units: Sv) in the 4-box model when considering enhanced vertical mixing in the subpolar ocean, forced by stochastic freshwater flux. Here, $M = 0.225$ ($\lambda = 9.45$ Sv kg^{-1} m^3); and the 4-box model is in a stable regime (region 1 in Fig. 9). (b),(c) The power spectra (units: dB) of AMOC anomalies and the noise, respectively. (d) The ratios of the AMOC spectrum to the stochastic freshwater spectrum (units: dB) with peaks around 0.003 cpy (330 years). In (b)–(d), thick curves represent ensemble mean, whose standard deviations are denoted by vertical short line segments. The black, green, and orange lines show results under red noise whose damping time scale are 1 month, 1 year, and 10 years, respectively.

Here, σ is given as 0.03, 0.005, and 0.001 psu yr^{-1}; correspondingly, α is set to 0.78, 0.98, and 0.998, respectively, giving an e-folding time of autocovariance function of about 1 month, 1 year, and 10 years, respectively. For each pair of parameters, 100 noise samples are generated. The 4-box model is integrated for 5000 years for each noise forcing, and the last 2000 years are used for analysis.

Forced by stochastic freshwater forcing (Fig. 10c), the 4-box model in region 1, which has only damped internal oscillations, exhibits sustained oscillation even in the presence of damping effect of nonlinear vertical mixing (Fig. 10a). The power spectrum of the forced AMOC anomaly suggests a multicentennial oscillation (Fig. 10b). The ratio of the AMOC spectrum to the freshwater spectrum is shown in Fig. 10d, which suggests that AMOC responds most efficiently to the noise whose period is about 330 years. This principal period is similar to the period from the linear analysis. Our study suggests that the multicentennial variation may be an intrinsic feature of the Atlantic Ocean, regardless of external forcing.

c. *Effect of nonlinear salinity advection*

The effect of nonlinear salinity advection (i.e., $q'\Delta S'$) on the oscillation behaviors in the box model is briefly examined in Fig. 11 by directly integrating the original Eq. (3), using the same parameters listed in Table 1. Without the enhanced vertical mixing, the nonlinearity will lead to a regime shift of the AMOC much faster than that in the linear system (Fig. 11a). However, in the presence of enhanced vertical mixing, the nonlinearity has nearly no effect on the oscillation in both amplitude and period (Fig. 11b). This is because, as mentioned previously, the enhanced vertical mixing is a critical stabilizing factor that can efficiently restrain the growth of perturbations, and the magnitude of $q'\Delta S'$ is always one order smaller than that of the other terms.

6. Summary

A self-sustained multicentennial oscillation of the AMOC is identified via a simplified modeling study. It is shown that the positive salinity advection feedback is important to the multicentennial oscillation. The enhanced mixing process in the subpolar ocean can be a critical mechanism to weaken the positive salinity advection feedback and limit the amplitude of the oscillation, ultimately leading to a self-sustained oscillation (Fig. 6). Mathematically, the oscillation period is determined by the eigenvalue of the system. Physically, it is determined by the turnover time of the upper-ocean water.

The enhanced mixing mechanism proposed in this work includes only two components: the mixing due to mesoscale and submesoscale eddies, and the diffusion related to the molecular to turbulent scale activities. Other processes, such as the

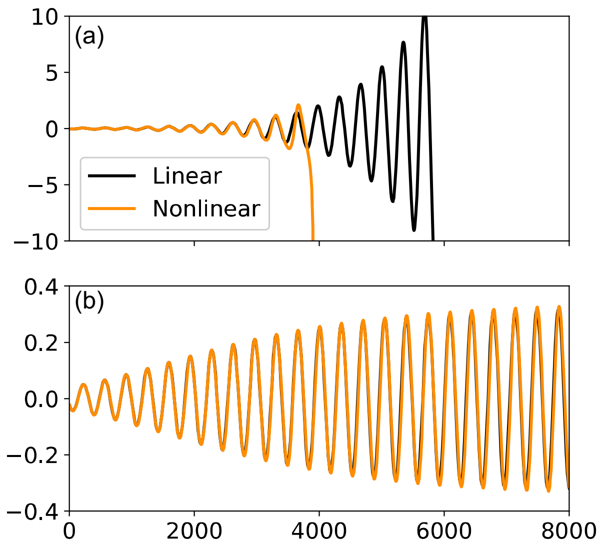

FIG. 11. Comparison between AMOC anomaly (units: Sv) obtained from time-forward integration of the original nonlinear Eq. (3) (orange) and corresponding linearized Eq. (7) (black), for oscillation (a) without considering enhanced vertical mixing in the subpolar box and (b) with enhanced vertical mixing.

rapid deep convection in the subpolar ocean, may have similar effects on the oscillation as vertical mixing. Deep convection is difficult to quantify in both models and real world, and it can be treated as an extreme vertical mixing event that happens in one time step in a box model as in Colin de Verdière et al. (2006). Our result suggests the eddy-induced mixing can influence the stability of the AMOC. Recent studies have shown that mesoscale turbulence may vary on climate time scale (Busecke and Abernathey 2019), and long-term variability can be damped by mesoscale turbulence (Sévellec et al. 2021). Further research is needed to quantify the role of turbulence on large-scale variability.

While both the enhanced mixing used in this paper and the nonlinear velocity closure used in RT97 can lead to a self-sustained oscillation by limiting the salinity advection feedback, these two mechanisms are different. In this paper, the enhanced mixing can transport salinity anomalies out of the subpolar upper ocean before the anomalies accumulate and lead to a bounded growth. The nonlinear velocity closure limits the development of perturbation flow so that it helps the system stay near its equilibrium. RT97 noted that the nonlinearity may come from internal nonlinear relation between large-scale meridional density gradient and AMOC strength. However, we prefer the enhanced mixing mechanism in maintaining the self-sustained oscillation of the system, since mixing processes, to some extent, are detectable and can be quantified in both observations and coupled models. In general, both the enhanced mixing and nonlinear volume transport closure can lead to a self-sustained oscillation. The two mechanisms are not contradictory. A combination of these two in a model may bring out more interesting results.

This study is motivated by the multicentennial variation of the AMOC found in a CESM control run (Fig. 1), which highlights the roles of internal processes in self-sustained oscillation. Bear in mind that external stochastic forcing can also excite a multicentennial oscillation in the box models (Fig. 10). It is still far from determined whether the multicentennial oscillation in our CESM control run is a self-sustained one. The simple model results in this work can be used to explain the oscillations in coupled climate models. However, its physics is too simple. Whether the mechanism of self-sustained oscillation is still valid in a system when more complex physics are considered needs to be investigated. For example, if temperature equation is included in the box model, does the self-sustained oscillation still exist? As described in the introduction, there are comprehensive studies on the stability and regime shift of the AMOC, and the centennial to millennium oscillations of the AMOC can be well identified (e.g., Sévellec et al. 2006, 2010). However, we would like to search for self-sustained multicentennial internal modes in a more realistic model, but not the oscillation with decaying or growing amplitude under external forcing. The existence of intrinsic modes of multicentennial time scale in the Atlantic Ocean may have profound implication for paleoclimatic studies and interpretations of the ongoing and future climate change.

Acknowledgments. This research is jointly supported by the NSF of China (41725021, 91737204, and 41376007) and by the foundation at the Shanghai Frontiers Science Center of Atmosphere–Ocean Interaction of Fudan University.

REFERENCES

Berner, K. S., N. Koç, F. Godtliebsen, and D. Divine, 2011: Holocene climate variability of the Norwegian Atlantic current during high and low solar insolation forcing. *Paleoceanography*, **26**, PA2220, https://doi.org/10.1029/2010PA002002.

Bonnet, R., and Coauthors, 2021: Increased risk of near term global warming due to a recent AMOC weakening. *Nat. Commun.*, **12**, 6108, https://doi.org/10.1038/s41467-021-26370-0.

Busecke, J., and R. P. Abernathey, 2019: Ocean mesoscale mixing linked to climate variability. *Sci. Adv.*, **5**, eaav5014, https://doi.org/10.1126/sciadv.aav5014.

Cessi, P., 1994: A simple box model of stochastically forced thermohaline flow. *J. Phys. Oceanogr.*, **24**, 1911–1920, https://doi.org/10.1175/1520-0485(1994)024<1911:ASBMOS>2.0.CO;2.

Chapman, M. R., and N. J. Shackleton, 2000: Evidence of 550-year and 1000-year cyclicities in North Atlantic circulation patterns during the Holocene. *Holocene*, **10**, 287–291, https://doi.org/10.1191/095968300671253196.

Colin de Verdière, A., M. B. Jelloul, and F. Sévellec, 2006: Bifurcation structure of thermohaline millennial oscillations. *J. Climate*, **19**, 5777–5795, https://doi.org/10.1175/JCLI3950.1.

Collins, M., and B. Sinha, 2003: Predictability of decadal variations in the thermohaline circulation and climate. *Geophys. Res. Lett.*, **30**, 1306, https://doi.org/10.1029/2002GL016504.

Cronin, T., K. Hayo, R. Thunell, G. Dwyer, C. Saenger, and D. Willard, 2010: The Medieval Climate Anomaly and Little Ice Age in Chesapeake Bay and the North Atlantic Ocean.

Palaeogeogr. Palaeoclimatol. Palaeoecol., **297**, 299–310, https://doi.org/10.1016/j.palaeo.2010.08.009.

Cubasch, U., R. Voss, G. C. Hegerl, J. Waskewitz, and T. J. Crowley, 1997: Simulation of the influence of solar radiation variations on the global climate with an ocean–atmosphere general circulation model. *Climate Dyn.*, **13**, 757–767, https://doi.org/10.1007/s003820050196.

Drijfhout, S. S., R. J. Haarsma, J. D. Opsteegh, and F. M. Selten, 1999: Solar induced versus natural variability in a coupled climate model. *Geophys. Res. Lett.*, **26**, 205–208, https://doi.org/10.1029/1998GL900277.

Fisher, D. A., 1982: Carbon-14 production compared to oxygen isotope records from Camp Century, Greenland and Devon Island, Canada. *Climatic Change*, **4**, 419–426, https://doi.org/10.1007/BF02423472.

Fox-Kemper, B., and R. Ferrari, 2008: Parameterization of mixed layer eddies. Part II: Prognosis and impact. *J. Phys. Oceanogr.*, **38**, 1166–1179, https://doi.org/10.1175/2007JPO3788.1.

——, ——, and R. W. Hallberg, 2008: Parameterization of mixed layer eddies. Part I: Theory and diagnosis. *J. Phys. Oceanogr.*, **38**, 1145–1165, https://doi.org/10.1175/2007JPO3792.1.

——, and Coauthors, 2011: Parameterization of mixed layer eddies. III: Implementation and impact in global ocean climate simulations. *Ocean Modell.*, **39**, 61–78, https://doi.org/10.1016/j.ocemod.2010.09.002.

Gajewski, K., 1988: Late Holocene climate changes in eastern North America estimated from pollen data. *Quat. Res.*, **29**, 255–262, https://doi.org/10.1016/0033-5894(88)90034-8.

Gent, P., and J. McWilliams, 1990: Isopycnal mixing in ocean circulation models. *J. Phys. Oceanogr.*, **20**, 150–155, https://doi.org/10.1175/1520-0485(1990)020<0150:IMIOCM>2.0.CO;2.

Griffies, S. M., and E. Tziperman, 1995: A linear thermohaline oscillator driven by stochastic atmospheric forcing. *J. Climate*, **8**, 2440–2453, https://doi.org/10.1175/1520-0442(1995)008<2440:ALTODB>2.0.CO;2.

Huang, R. X., 1994: Thermohaline circulation: Energetics and variability in a single-hemisphere basin model. *J. Geophys. Res.*, **99**, 12 471–12 485, https://doi.org/10.1029/94JC00522.

——, J. R. Luyten, and H. M. Stommel, 1992: Multiple equilibrium states in combined thermal and saline circulation. *J. Phys. Oceanogr.*, **22**, 231–246, https://doi.org/10.1175/1520-0485(1992)022<0231:MESICT>2.0.CO;2.

Jiang, W., G. Gastineau, and F. Codron, 2021: Multicentennial variability driven by salinity exchanges between the Atlantic and the Arctic Ocean in a coupled climate model. *J. Adv. Model. Earth Syst.*, **13**, e2020MS002366, https://doi.org/10.1029/2020MS002366.

Johnsen, S. J., W. Dansgaard, H. B. Clausen, and C. C. Langway, 1970: Climatic oscillations 1200–2000 AD. *Nature*, **227**, 482–483, https://doi.org/10.1038/227482a0.

LaMarche, V. C., 1974: Paleoclimatic inferences from long tree-ring records: Intersite comparison shows climatic anomalies that may be linked to features of the general circulation. *Science*, **183**, 1043–1048, https://doi.org/10.1126/science.183.4129.1043.

Marotzke, J., 1990: Instabilities and multiple equilibria of the thermohaline circulation. Ph.D. thesis, Christian-Albrechts-Universität, 126 pp.

——, 1996: Analysis of thermohaline feedbacks. *Decadal Climate Variability: Dynamics and Predictability*, D. L. T. Anderson and J. Willebrand, Eds., Springer, 333–378.

——, and P. Stone, 1995: Atmospheric transports, the thermohaline circulation, and flux adjustments in a simple coupled model. *J. Phys. Oceanogr.*, **25**, 1350–1364, https://doi.org/10.1175/1520-0485(1995)025<1350:ATTTCA>2.0.CO;2.

Miettinen, A., D. V. Divine, K. Husum, N. Koç, and A. Jennings, 2015: Exceptional ocean surface conditions on the SE Greenland shelf during the medieval climate anomaly. *Paleoceanography*, **30**, 1657–1674, https://doi.org/10.1002/2015PA002849.

Mikolajewicz, U., and E. Maier-Reimer, 1990: Internal secular variability in an ocean general circulation model. *Climate Dyn.*, **4**, 145–156, https://doi.org/10.1007/BF00209518.

Miller, G. H., and Coauthors, 2012: Abrupt onset of the Little Ice Age triggered by volcanism and sustained by sea-ice/ocean feedbacks. *Geophys. Res. Lett.*, **39**, L02708, https://doi.org/10.1029/2011GL050168.

Moffa-Sánchez, P., I. R. Hall, D. J. Thornalley, S. Barker, and C. Stewart, 2015: Changes in the strength of the Nordic seas overflows over the past 3000 years. *Quat. Sci. Rev.*, **123**, 134–143, https://doi.org/10.1016/j.quascirev.2015.06.007.

——, and Coauthors, 2019: Variability in the northern North Atlantic and Arctic Oceans across the last two millennia: A review. *Paleoceanogr. Paleoclimatol.*, **34**, 1399–1436, https://doi.org/10.1029/2018PA003508.

Moreno-Chamarro, E., D. Zanchettin, K. Lohmann, and J. H. Jungclaus, 2017: An abrupt weakening of the subpolar gyre as trigger of Little Ice Age-type episodes. *Climate Dyn.*, **48**, 727–744, https://doi.org/10.1007/s00382-016-3106-7.

Msadek, R., and C. Frankignoul, 2008: Atlantic multidecadal oceanic variability and its influence on the atmosphere in a climate model. *Climate Dyn.*, **33**, 45–62, https://doi.org/10.1007/s00382-008-0452-0.

Mysak, L. A., T. F. Stocker, and F. Huang, 1993: Century-scale variability in a randomly forced, two-dimensional thermohaline ocean circulation model. *Climate Dyn.*, **8**, 103–116, https://doi.org/10.1007/BF00208091.

Nakamura, M., P. H. Stone, and J. Marotzke, 1994: Destabilization of the thermohaline circulation by atmospheric eddy transports. *J. Climate*, **7**, 1870–1882, https://doi.org/10.1175/1520-0442(1994)007<1870:DOTTCB>2.0.CO;2.

Rind, D., J. Lean, and R. Healy, 1999: Simulated time-dependent climate response to solar radiative forcing since 1600. *J. Geophys. Res.*, **104**, 1973–1990, https://doi.org/10.1029/1998JD200020.

Risebrobakken, B., E. Jansen, C. Andersson, E. Mjelde, and K. Hevrøy, 2003: A high-resolution study of Holocene paleoclimatic and paleoceanographic changes in the Nordic seas. *Paleoceanography*, **18**, 1017, https://doi.org/10.1029/2002PA000764.

Rivin, I., and E. Tziperman, 1997: Linear versus self-sustained interdecadal thermohaline variability in a coupled box model. *J. Phys. Oceanogr.*, **27**, 1216–1232, https://doi.org/10.1175/1520-0485(1997)027<1216:LVSSIT>2.0.CO;2.

Roebber, P. J., 1995: Climate variability in a low-order coupled atmosphere–ocean model. Tellus, **47A**, 473–494, https://doi.org/10.3402/tellusa.v47i4.11534.

Rooth, C., 1982: Hydrology and ocean circulation. *Prog. Oceanogr.*, **11**, 131–149, https://doi.org/10.1016/0079-6611(82)90006-4.

Sakai, K., and W. R. Peltier, 1999: A dynamical systems model of the Dansgaard-Oeschger oscillation and the origin of the bond cycle. *J. Climate*, **12**, 2238–2255, https://doi.org/10.1175/1520-0442(1999)012<2238:ADSMOT>2.0.CO;2.

Sévellec, F., and A. V. Fedorov, 2014: Millennial variability in an idealized ocean model: Predicting the AMOC regime shifts. *J. Climate*, **27**, 3551–3564, https://doi.org/10.1175/JCLI-D-13-00450.1.

——, T. Huck, and M. Ben Jelloul, 2006: On the mechanism of centennial thermohaline oscillations. *J. Mar. Res.*, **64**, 355–392, https://doi.org/10.1357/002224006778189608.

——, ——, and A. Colin de Verdière, 2010: From centennial to millennial oscillation of the thermohaline circulation. *J. Mar. Res.*, **68**, 723–742, https://doi.org/10.1357/002224011795977635.

——, A. Garabato, and T. Huck, 2021: Damping of climate-scale oceanic variability by mesoscale eddy turbulence. *J. Phys. Oceanogr.*, **51**, 491–503, https://doi.org/10.1175/JPO-D-20-0141.1.

Sicre, M.-A., I. R. Hall, J. Mignot, M. Khodri, U. Ezat, M.-X. Truong, J. Eiríksson, and K.-L. Knudsen, 2011: Sea surface temperature variability in the subpolar Atlantic over the last two millennia. *Paleoceanography*, **26**, PA4218, https://doi.org/10.1029/2011PA002169.

Sirén, G., 1961: Skogsgränstallen som indikator för klimatfluktuationerna i norra Fennoskandien under historisk tid [The tree-limit pine as an indicator of climate fluctuations in northern Fennoscandia during historical time]. *Commun. Inst. For. Fenn.*, **54**, 1–66.

Soutar, A., and J. D. Isaacs, 1969: History of fish populations inferred from fish scales in anaerobic sediments off California. *CCOFI Rep.*, **13**, 63–70.

Stocker, T. F., and L. A. Mysak, 1992: Climatic fluctuations on the century time scale: A review of high-resolution proxy data and possible mechanisms. *Climatic Change*, **20**, 227–250, https://doi.org/10.1007/BF00139840.

Stommel, H., 1961: Thermohaline convection with two stable regimes of flow. *Tellus*, **13**, 224–230, https://doi.org/10.3402/tellusa.v13i2.9491.

Stuiver, M., and T. Braziunas, 1989: Atmospheric ^{14}C and century-scale solar oscillations. *Nature*, **338**, 405–408, https://doi.org/10.1038/338405a0.

Tziperman, E., and P. Ioannou, 2002: Transient growth and optimal excitation of thermohaline variability. *J. Phys. Oceanogr.*, **32**, 3427–3435, https://doi.org/10.1175/1520-0485(2002)032<3427:TGAOEO>2.0.CO;2.

——, J. R. Toggweiler, Y. Feliks, and K. Bryan, 1994: Instability of the thermohaline circulation with respect to mixed boundary conditions: Is it really a problem for realistic models? *J. Phys. Oceanogr.*, **24**, 217–232, https://doi.org/10.1175/1520-0485(1994)024<0217:IOTTCW>2.0.CO;2.

Weber, S. L., T. J. Crowleyand, and G. V. D. Schrier, 2004: Solar irradiance forcing of centennial climate variability during the Holocene. *Climate Dyn.*, **22**, 539–553, https://doi.org/10.1007/s00382-004-0396-y.

Welander, P., 1982: A simple heat-salt oscillator. *Dyn. Atmos. Oceans*, **6**, 233–242, https://doi.org/10.1016/0377-0265(82)90030-6.

——, 1986: Thermohaline effects in the ocean circulation and related simple model. *Large Scale Transport Processes in Oceans and Atmosphere*, J. Willebrand and D. L. T. Anderson, Eds., D. Reidel, 163–200.

Winton, M., and E. S. Sarachik, 1993: Thermohaline oscillations induced by strong steady salinity forcing of ocean general circulation models. *J. Phys. Oceanogr.*, **23**, 1389–1410, https://doi.org/10.1175/1520-0485(1993)023<1389:TOIBSS>2.0.CO;2.

Yang, H., Q. Li, K. Wang, Y. Sun, and D. Sun, 2015: Decomposing the meridional heat transport in the climate system. *Climate Dyn.*, **44**, 2751–2768, https://doi.org/10.1007/s00382-014-2380-5.

——, Y. Zhao, and Z. Liu, 2016: Understanding Bjerknes compensation in atmosphere and ocean heat transports using a coupled box model. *J. Climate*, **29**, 2145–2160, https://doi.org/10.1175/JCLI-D-15-0281.1.

Zhang, R., M. Follows, and J. Marshall, 2002: Mechanisms of thermohaline mode switching with application to warm equable climates. *J. Climate*, **15**, 2056–2072, https://doi.org/10.1175/1520-0442(2002)015<2056:MOTMSW>2.0.CO;2.

Zhao, Y., H. Yang, and Z. Liu, 2016: Assessing Bjerknes compensation for climate variability and its time-scale dependence. *J. Climate*, **29**, 5501–5512, https://doi.org/10.1175/JCLI-D-15-0883.1.

Zheng, J., X. Shao, Z. Hao, and Q. Ge, 2010: An overview of research on climate change in China during the past 2000 years (in Chinese). *Geogr. Res.*, **29**, 1561–1570.